JACS
JOURNAL OF THE AMERICAN CHEMICAL SOCIETY
Communication
pubs.acs.org/JACS

T_c Maximum in Solid Solution of Pyrite $IrSe_2$–$RhSe_2$ Induced by Destabilization of Anion Dimers

Jiangang Guo,[†] Yanpeng Qi,[†] Satoru Matsuishi,[‡] and Hideo Hosono*[,†,‡]

[†]Frontier Research Center and [‡]Materials and Structures Laboratory, Tokyo Institute of Technology, Yokohama 226-8503, Japan

Supporting Information

ABSTRACT: We have established a well-defined dome-shaped T_c curve in $Ir_{0.94-x}Rh_xSe_2$ superconductors. The maximum T_c^{onset} of 9.6 K was obtained at x = 0.36, at which the Se–Se separation in the dimer anion is the longest. Simultaneously, the destabilization of Se–Se dimers accompanied by partial electron transfer from the Ir/Rh to the chalcogenide ions resulted in the emergence of optimal T_c.

Exploring a novel parent compound and then regulating its superconductivity has been a long-standing challenge in the materials community. The superconducting critical temperature (T_c) of cuprates and iron-based superconductors, although not yet clearly understood, should have intimate correlation with local structure distortion. Experimentally, their T_c^{max} values are proportional to the number of CuO_2 layers and regular degree of FeX_4 (X = As, Se) tetrahedrons, respectively.[1,2] In particular, the isovalent substitution of Te/P for Se/As in iron-based superconductors demonstrated that symmetry of local atomic structure not only could drastically enhance the scale of T_c as well, but also could profoundly influence the normal-state transport properties.[3,4] Recently, as a structural parameter, the dimerization has been reported in the low-temperature insulting phase of three-dimensional $CuIr_2S_4$, which resulted in spin singlets and was responsible for the strong loss of magnetic moment.[5] Also, breaking the molecule-like anion dimer in $SrCo_2(Ge_{1-x}P_x)_2$ successfully induced the unexpected ferromagnetic quantum critical point between both paramagnetic end members.[6]

Pyrite $TMCh_2$ (TM = transition metal; Ch = chalcogenide atom) is another kind of dimer-containing compound, in which strong p–p hybridization within the Ch–Ch pairs acts as divalent Ch_2^{2-}, and the transition metal formally adopts the TM^{2+} cation.[7,8] Its unique Ch_2^{2-} dimer and metal-cation sublattices arrange themselves in an interpenetrating face-centered-cubic geometry (see Figure 1d). The geometry of the dimer not only strongly modifies the crystallographic structure but also tunes the number of electrons in the high-energy orbital. Very recently, we have discovered that pyrite Ir_xSe_2 is a superconductor, of which the normal-state resistivity maintains a non-metal behavior and T_c increases monotonically to ~6 K as the scale of the unit cell and bond length of the Ch_2^{2-} dimer expand.[9] This discovery offers a rare opportunity to investigate the superconductivity and normal-state properties by tuning the bonding state of Se–Se dimers in pyrite compounds. In this Communication, we describe a well-defined dome shape of T_c responding to negative chemical pressure in $Ir_{0.94-x}Rh_xSe_2$ superconductors. The normal-state resistivity evolves from non-metal to strange metal, and then to classic Fermi liquid metal. Moreover, the specific heat capacity measurement demonstrated that $Ir_{0.58}Rh_{0.36}Se_2$ exhibits maximal T_c, ~9.6 K, accompanied by the weakening of the dimer bonding and possible structural instability.

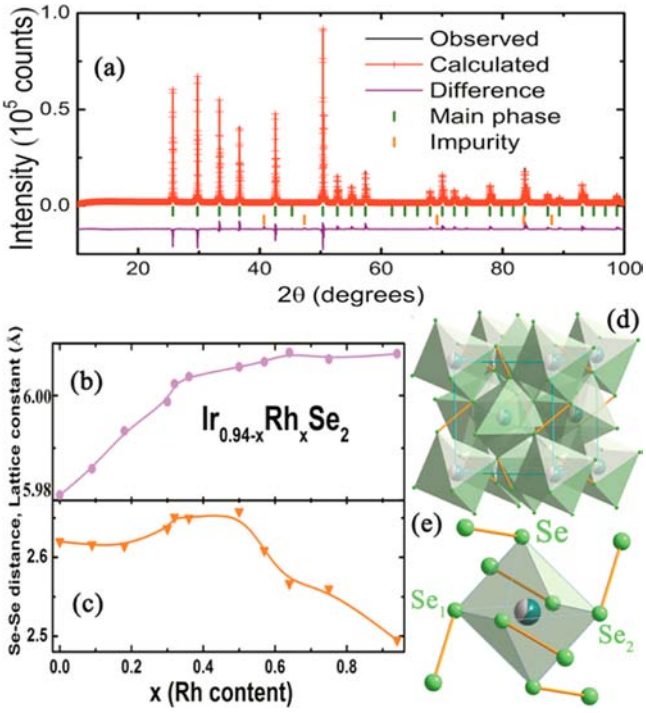

Figure 1. Powder X-ray diffraction pattern and crystal structure of $Ir_{0.94-x}Rh_xSe_2$. (a) Observed and fitted XRD patterns of $Ir_{0.58}Rh_{0.36}Se_2$. The result of the Rietveld refinement showed good convergence (R_{wp} = 5.92%, R_p = 4.53%). (b,c) Variation of the lattice constant and the Se–Se dimer distance. (d) Crystal structure of $Ir_{0.94-x}Rh_xSe_2$ solid-state solution. The MSe_6 octahedrons are connected by the Se–Se dimers (yellow bonds). (e) A fragment of the MSe_6 octahedron, where all corners are bonded with Se–Se dimers. $Se–Se_1$ and $Se–Se_2$ denote two types of Se–Se bond in one octahedron.

The starting materials—Ir, Rh, and Se powders—were mixed well and loaded into the h-BN capsule in an Ar-filled glovebox (O_2, H_2O < 1 ppm). The assembly was then subjected to a belt-type high-pressure machine at ~5 GPa and ~1773 K for 2 h.

Received: October 2, 2012
Published: November 27, 2012

The as-prepared samples were characterized by powder X-ray diffraction (PXRD) using a Bruker D8 Advance with Cu Kα radiation. Rietveld refinements of the data were performed with the TOPAS package.[10] The electrical resistivity was measured through the standard four-wire method on the physical property measurement system (PPMS, Quantum Design). Specific heat measurement was performed by the thermal relaxation method in the temperature range of 1.8−20 K (PPMS, Quantum Design). The dc magnetic properties were characterized using a vibrating sample magnetometer (VSM, Quantum Design). The chemical compositions of the samples were examined by electron probe microscope analysis (EPMA) in backscattered electron (BSE) mode.

Figure 1a shows the measured PXRD pattern and Rietveld refinement results for $Ir_{0.58}Rh_{0.36}Se_2$ as a representative composition. Except for slight Ir metal impurity, all the reflections could be indexed with a cubic cell of parameters $a = b = c = 6.00365(2)$ Å, $V = 216.394(4)$ Å^3. Examination of diffraction extinction revealed that all of the samples crystallized in a primitive lattice with a probable space group of $Pa\bar{3}$ (No. 205), and the Rietveld refinement confirmed that the crystal structure was isostructural to our previous data.[9] As shown in Figure 1b, the size of the unit cell could continuously increase with the substitution of Rh for Ir. For $x < 0.65$, the lattice constant increased monotonically to 6.00825(2) Å, and then it slowly became saturated at the higher Rh content. Following a simple ionic model, their unit cell dimension should decrease with increasing Rh. Thus, this unexpected increase suggests that the effect of the crystal electric field and Se_2^{2-} polarization needs to be taken into account, as proposed by Birkholz.[11,12] Regarding to the critical parameters, the distance of Se−Se dimers and the octahedral MSe_6 (M = Ir or Rh) unit are shown in Figure 1c and e, respectively. The bond length of the Ch_2^{2-} dimer slowly increased to the maximum of ∼2.65 Å and then drastically decreased for $x > 0.5$, implying that rhodium substitution could effectively control the nonbonded and bonded states of the dimers. At the same time, we could obtain bonding information on the MSe_6 octahedron from the Rietveld refinement (see Figure S1). The Rh substitution elongated all bonds, i.e., M−Se, Se_1−Se, and Se_2−Se, and substantially enlarged the size of the MSe_6 octahedron, which is the possible origin of anomalous lattice expansion. Density functional theory (DFT) calculations show that the width of the energy band near the Fermi level gradually decreases with x (see Figure S2). Thus, the structural analysis indicated that the transition in $Ir_{0.94-x}Rh_xSe_2$ is continuous in nature.

Figure 2a,b shows the temperature dependence of electrical resistivity under a zero field below 305 and 12 K. Let us first focus on the normal-state transport properties of $Ir_{0.94-x}Rh_xSe_2$ with $0 \le x \le 0.94$. As shown in Figure 2a, the parent compound showed a negative temperature coefficient at higher temperature, suggesting its normal-state property as a non-metal or semiconductor. With further substitution, thermal coefficients of the normal-state resistivity slowly became positive, corresponding to metal behavior. We used the power-law equation $\rho(T) = \rho_0 + AT^{\alpha}$ (ρ_0 is residual resistivity; A is a constant) to fit all normal-state resistivity curves up to 200 K. The plot of the obtained value α versus rhodium composition is shown in Figure 2c. With increasing x, α gradually increases to 1 at the intermediate range, and then approaches 2 for the $Rh_{0.94}Se_2$ end member. For $x = 0.36$, one can observe nearly perfect T-linear resistivity dependence at a wide temperature range above T_c, which strikingly deviates

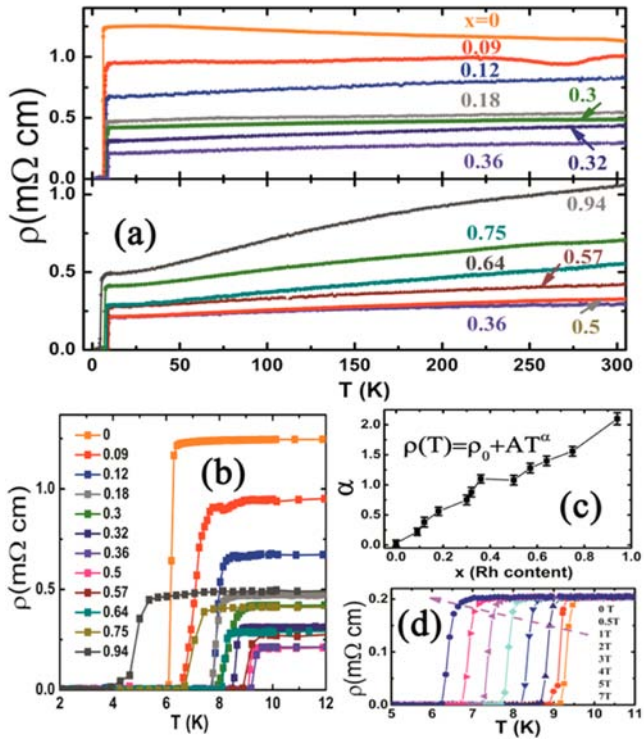

Figure 2. (a,b) Temperature dependence of electrical resistivity under zero magnetic field below 305 and 12 K, respectively. (c) The value of α obtained from the fitting results of normal-state electrical resistivity. (d) Resistivity of $Ir_{0.58}Rh_{0.36}Se_2$ under various magnetic fields.

from the classic Fermi-liquid theory. It is evident that electron−phonon scattering dominates the process of conductivity. Thus, as x increases, the normal-state transport property evolves from non-metal to T-linear resistivity, and finally to a classic metal.

Figure 2b shows the superconducting properties for the lower-temperature zone. It can be seen that the resistivity abruptly dropped to zero. In addition, the fact that T_c first increased and then decreased with increasing x is clearly shown. The maximal T_c^{onset}, 9.6 K, occurred at $x = 0.36$, which corresponds to the linear-resistivity temperature dependence. The T_c of $RhSe_2$ agrees with the previous report.[13] It is worth noting that the anomalous T-linear resistivity behavior is seen for the region of the maximal T_c. This correspondence between the region at which T-linear dependence of ρ in the normal state and the optimal T_c region has been reported in cuprates and iron-based superconductors.[14,15] Figure 2d shows the resistivity of $Ir_{0.58}Rh_{0.36}Se_2$ under different magnetic fields. The transition was suppressed by applying external magnetic fields. The estimated upper critical fields H_{c2} were 28.5 and 24.5 T from the WHH model[16] and Ginzburg−Landau equation, respectively (see Figure S3c).

The enhanced superconductivity was further demonstrated by the low-temperature magnetic susceptibility and heat capacity. Figure 3a,b shows that a large diamagnetic signal—evidence of bulk superconductivity—was observed in all samples. The variation and the maximal value of T_c were consistent with the above electrical measurement. The estimated lower critical field H_{c1} was about 200 Oe from the isothermal magnetization curve, indicating that the material is a type-II superconductor (see Figure S3).

Further investigation of the superconducting phase and lattice vibration were carried out by heat capacity measurement.

dx.doi.org/10.1021/ja309724w | J. Am. Chem. Soc. 2012, 134, 20001−20004

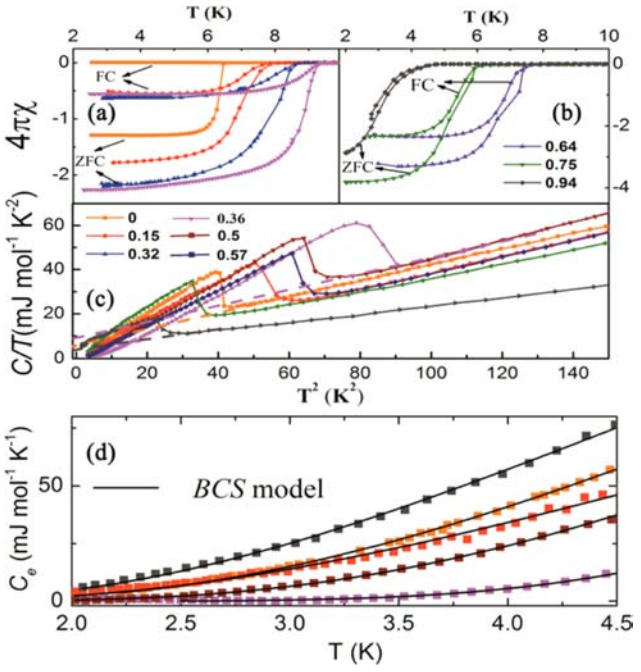

Figure 3. (a,b) Temperature dependences of magnetic properties at a magnetic field H of 10 Oe for $Ir_{0.94-x}Rh_xSe_2$ in zero-field-cooling (ZFC) and field-cooling (FC) processes. (c) Total heat capacity divided by T as a function of temperature squared. The dashed lines are the extrapolated line from Debye model fitting. (d) Temperature dependence of the electronic specific heat; the solid line is the conventional BCS model fitting result.

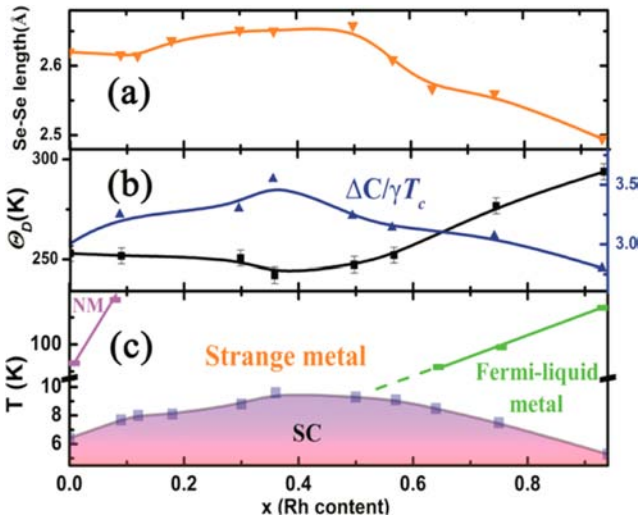

Figure 4. Summary and phase diagram of $Ir_{0.94-x}Rh_xSe_2$. (a) Variation of the Se−Se dimer bond length. (b) Debye temperature Θ_D and $\Delta C/\gamma T_c$ as a function of rhodium content x. (c) Electronic phase diagram of $Ir_{0.94-x}Rh_xSe_2$. The violet symbol denotes the crossover temperature from the non-metal (NM) to the strange-metal state. The green symbol denotes the crossover temperature from the strange-metal to the classic Fermi-liquid-metal state.

From Figure 3c, we can see that the large superconducting jump for x = 0.36 coincides with the $\rho(T)$ and $\chi(T)$ data. We could easily fit these curves above T_c with the Debye model $C_p/T = \gamma + \beta T^2$, in which γ is the Sommerfeld electronic coefficient and the other term is the lattice contribution. From the intercept of plots, we found that the electronic coefficients are 6.41, 8.02, and 3.57 $mJ{\cdot}mol^{-1}{\cdot}K^{-2}$ for x = 0, 0.36, and 0.94, respectively. Following the free electron model, the density of states (DOS) values at Fermi energy, $N(E_F) = 3\gamma/\pi^2 K_B^2$, are calculated as 2.64, 3.3, and 1.47 $states{\cdot}eV^{-1}{\cdot}f.u.^{-1}$, respectively. Density functional calculations (see Figure s2) show that the Fermi energy of $Ir_{0.5}Rh_{0.5}Se_2$ locates at the peak of the DOS, which is consistent with the observed data.

The value of slopes β was largest (0.41 $mJ{\cdot}mol^{-1}{\cdot}K^{-4}$) for x = 0.36. We plotted the Debye temperature, Θ_D, evaluated from the equation $\Theta_D = (12\pi^4 nR/5\beta)^{1/3}$, as a function of x in Figure 4b. The Θ_D of intermediate compositions reached a minimum value, ~242 K. Since the Debye frequency is proportional to the Debye temperature, we deduced there may be an occurrence of phonon softening from the reduced frequency. The softer phonon mode possibly implies that the crystal structure approached the structural instability states.

In Figure 3d, we show the electronic-specific heat $C_e = C_{total} - C_{phonon}$ versus T, where C_{phonon} comes from the Debye model results. The s-wave BCS fitting of C_e vs T curves[17] gave $2\Delta/k_BT_c$ = 5.95 for x = 0.36, suggesting that the coupling state was the strongest for the weaken dimer. As the dimers close, the whole system gradually transits to the classic BCS weak coupling state (see Figure S4). Moreover, the normalized heat capacity jump $\Delta C/\gamma T_c$ exhibited a similar trend, and also reached the maximal value 3.55 at x = 0.36, as shown in Figure 4b. Therefore, we could safely infer the rarely critical nature by modifying the bonding state of the dimers, indicative of T_c, γ, and the Debye temperature in $Ir_{0.94-x}Rh_xSe_2$.

The main results are summarized in Figure 4 as an electronic phase diagram. With increasing bond length of dimer, both the Θ_D and T_c of $Ir_{0.94-x}Rh_xSe_2$ slowly approach their extremes. It should be noted that at the lowest Debye temperature, the largest $\Delta C/\gamma T_c$ and T_c emerge at the vicinity of the weakening dimer states. As the dimer bonding is enhanced again, T_c starts to decrease, and the high-frequency lattice vibration is recovered. The present data clearly show that the bonding strength in dimer states in $Ir_{0.94-x}Rh_xSe_2$ is correlated with a dome-shaped T_c curve and significantly influences the lattice vibration. It has been reported that $BaNi_2(As_{1-x}P_x)_2$ shows sudden phonon softening when the lower-T_c triclinic phase was converted to a higher-T_c tetragonal phase by isovalent substitution, even though the $N(E_F)$ was independent of doped content.[18] Furthermore, the T_c of $BaSi_2$ could be enhanced from 6 to 8.9 K by flattening the Si planes, which appeared at the structural instability state involving softening of the Si phonon mode.[19] In the present case, the combined results demonstrated that the charge fluctuation between the Se_2^{2-} dimer and cation essentially rises as the dimer bonding gradually weakens, which is responsible for the increment of γ. The PDOS pattern around the Fermi energy shows that the contribution of the Se orbital increases whereas that of transition metal keeps almost constant with increasing Ir content, indicating that the hybridization state of Ir/Rh-d and Se-4p orbitals becomes stronger. Although the DOS shows the maximal value at x = 0.36, there could be nother possibilities resulting in the significant enhancement of T_c (superconducting gap), such as strengthening of electron−phonon coupling and softening of the phonon due to the structural instability at the edge of weak dimer states. Further phonon spectrum calculations will be required to validate the proposed mechanism.

To summarize, we found a domed T_c curve in $Ir_{0.94-x}Rh_xSe_2$ by tuning the bonding state of Se_2^{2-} dimers. At the optimal T_c,

dx.doi.org/10.1021/ja309724w | J. Am. Chem. Soc. 2012, 134, 20001−20004

the Ch−Ch separation, electronic density of states, and $\Delta C/\gamma T_c$ all reach their maximal values. In addition, the normal-state resistivity shows T-linear dependence in the range of the weakening dimer, and then approaches that of a conventional metal with the shortening of the dimer. These results suggest that a transition metal pyrite is a good platform for superconductivity to emerge from modification of the bonding state of the dimer anions.

■ ASSOCIATED CONTENT

Supporting Information

Bond parameters of MSe_6 octahedra, isothermal magnetization and critical fields of $Ir_{0.58}Rh_{0.36}Se_2$, fitting results of C_e vs T curves, and DFT calculation detail and results. This material is available free of charge via the Internet at http://pubs.acs.org.

■ AUTHOR INFORMATION

Corresponding Author

hosono@msl.titech.ac.jp

Notes

The authors declare no competing financial interest.

■ ACKNOWLEDGMENTS

We acknowledge Dr. H. Lei and Mr. S. Iimura for valuable discussions. This work was supported by the Funding Program for World-Leading Innovative R&D on Science and Technology (FIRST), Japan.

■ REFERENCES

(1) Scott, B. A; Suard, E. Y.; Tsuei, C. C.; Mitzi, D. B.; McGuire, T. R.; Chen, B.-H.; Walker, D. *Physica C* **1994**, *230*, 239.
(2) Kamihara, Y.; Watanabe, T.; Hirano, M.; Hosono, H. *J. Am. Chem. Soc.* **2008**, *130*, 3296. Lee, C. H.; Kihou, K.; Iyo, A.; Kito, H.; Shirage, P. M.; Eisaki, H. *Solid State Commun.* **2012**, *152*, 644. Zhao, J.; Huang, Q.; de la Cruz, C.; Li, S. L.; Lynn, J. W.; Chen, Y.; Green, M. A.; Chen, G. F.; Li, G.; Li, Z.; Luo, J. L.; Wang, N. L.; Dai, P. C. *Nat. Mater.* **2008**, *7*, 953.
(3) Kasahara, S.; Shibauchi, T.; Hashimoto, K.; Ikada, K.; Tonegawa, S.; Okazaki, R.; Shishido, H.; Ikeda, H.; Takeya, H.; Hirata, K.; Terashima, T.; Matsuda, Y. *Phys. Rev. B* **2010**, *81*, 184519.
(4) Zajdel, P.; Hsieh, P.-Y.; Rodriguez, E. E.; Butch, N. P.; Magill, J. D.; Paglione, J.; Zavalij, P.; Suchomel, M. R.; Green, M. A. *J. Am. Chem. Soc.* **2010**, *132*, 13000.
(5) Radaelli, P. G.; Horibe, Y.; Gutmann, M. J.; Ishibashi, H.; Chen, C. H.; Ibberson, R. M.; Koyama, Y.; Hor, Y. S.; Kiryukhin, V.; Cheong, S. W. *Nature* **2002**, *416*, 155.
(6) Jia, S.; Jiramongkolchai, P.; Suchomel, M. R.; Toby, B. H.; Checkelsky, J. G.; Ong, N. P.; Cava, R. *J. Nat. Phys.* **2011**, *7*, 207.
(7) Hu, J.; Zhang, Y.; Law, M.; Wu, R. *J. Am. Chem. Soc.* **2012**, *134*, 13219.
(8) Honigl, J. M.; Spalek, J. *Chem. Mater.* **1998**, *10*, 2910.
(9) Qi, Y. P.; Matsuishi, S.; Guo, J. G.; Mizoguchi, M.; Hosono, H. *Phys. Rev. Lett.* **2012**, in press.
(10) *TOPAS*, Version 3; Bruker AXS: Karlsruhe, Germany, 2005.
(11) Birkholz, M.; Fiechter, S.; Hartmann, A.; Tributsch, H. *Phys. Rev. B* **1991**, *43*, 11926.
(12) Birkholz, M.; Rudert, R. *Phys. Stat. Sol. (b)* **2008**, *245*, 1858.
(13) Gelle, S.; Cetlin, B. B. *Acta Crystallogr.* **1955**, *8*, 272.
(14) Jin, K.; Butch, N. P.; Kirshenbaum, K.; Paglione, J.; Greene, R. L. *Nature* **2011**, *476*, 73.
(15) Rullier-Albenque, F.; Colson, D.; Forget, A.; Alloul, H. *Phys. Rev. Lett.* **2009**, *103*, 057001.
(16) Werthamer, N. R.; Helfand, E.; Hohenberg, P. C. *Phys. Rev.* **1966**, *147*, 295.
(17) Klimczuk, T.; Ronning, F.; Sidorov, V.; Cava, R. J.; Thompson, J. D. *Phys. Rev. Lett.* **2007**, *99*, 257004.
(18) Kudo, K.; Takasuga, M.; Okamoto, Y.; Hiroi, Z.; Nohara, M. *Phys. Rev. Lett.* **2012**, *109*, 097002.
(19) Flores-Livas, J. A.; Debord, R.; Botti, S.; San Miguel, A.; Marques, M. A. L.; Pailhes, S. *Phys. Rev. Lett.* **2011**, *106*, 087002.